Wireless resonant circuits for minimally invasive sensing of biophysical processes in magnetic resonance imaging

Citation: Hai, Aviad et al., "Wireless resonant circuits for the minimally invasive sensing of biophysical processes in magnetic resonance imaging." Nature Biomedical Engineering 3, 1 (January 2019): 69–78 ©2018 Authors

As Published: https://dx.doi.org/10.1038/S41551-018-0309-8

Publisher: Springer Nature

Persistent URL: https://hdl.handle.net/1721.1/130317

Version: Author's final manuscript: final author's manuscript post peer review, without publisher's formatting or copy editing

Wireless resonant circuits for minimally invasive sensing of biophysical processes in magnetic resonance imaging

Aviad Hai[1], Virginia Ch. Spanoudaki[2], Benjamin B. Bartelle[1], Alan Jasanoff[1,3,4]

[1] Department of Biological Engineering,
[2] Koch Institute for Integrative Cancer Research,
[3] Department of Brain & Cognitive Sciences,
[4] Department of Nuclear Science & Engineering
Massachusetts Institute of Technology
77 Massachusetts Ave.
Rm. 16-561
Cambridge, MA 02139

Correspondence to AJ (*jasanoff@mit.edu*)

Submission date: 8/29/18

Abbreviations: Adenosine Triphosphate (ATP), Drain-Source Voltage (V_{DS}), Field Effect Transistor (FET), Field of View (FOV), Functional Magnetic Resonance Imaging (fMRI), Gate-Source Voltage (V_{GS}), Implantable Active Coil-based Transducer (ImpACT), Magnetic Resonance Imaging (MRI), Photons Per Second (p/s), Photosensitive Field Effect Transistor (PhotoFET), Quality Factor (Q), Radiofrequency (RF), Resistor-Inductor-Capacitor (RLC), Resonant Frequency (ν), Signal-to-Noise Ratio (SNR), Specific Absorption Rate (SAR), Longitudinal Relaxation Time (T_1), Transverse Relaxation Time (T_2)

ABSTRACT

Biological electromagnetic fields arise throughout all tissue depths and types, and they correlate with physiological processes and signaling in diverse organs of the body. Most methods for monitoring these fields are either highly invasive or spatially coarse, however. Probes for sensitizing noninvasive imaging to biogenic fields could bypass these limitations. Here we meet the need for such probes by introducing implantable, active, coil-based transducers (ImpACTs) that are detectable in magnetic resonance imaging (MRI). ImpACT devices consist of inductively coupled, resonant circuits that change their properties in response to electrical or photonic cues, thereby modulating local MRI signal without need for onboard power or wired connectivity. We discuss design parameters relevant to construction of ImpACTs on millimeter and submillimeter scales, and we demonstrate *in vivo* functionality of an ImpACT for measuring time-resolved bioluminescence in rodent brains. Biophysical sensing via microcircuits that leverage the potent capabilities of MRI may enable a wide range of biological and biomedical applications.

INTRODUCTION

Biogenic electromagnetic fields underlie many of the body's most important processes, and form the basis of crucial biomedical technologies for monitoring and diagnosis[1-4]. In nervous and muscular tissue, electrical potentials are essential to rapid intercellular communication and changes in cellular state[5-7]. Measuring such signals is fundamental for the study of healthy brain and muscle function, and for characterizing threatening dysfunctions such as those that occur in epilepsy or peripheral neuropathies[8-10]. Many chemical

processes can also be converted into electromagnetic signals using electrochemical techniques. In both preclinical research and clinical settings, such strategies are the basis for monitoring tissue variables ranging from pH in tumors[11, 12] to neurochemical disruptions in Parkinson's disease[13-15]. Although visible photonic signals do not arise endogenously in mammals, detection of such signals in deep tissue is the basis for studies of gene expression and biochemical activity via bioluminescent and chemiluminescent reporters in animal models[16, 17]. A minimally-invasive technology for improved measurement of optical signals near their origin could vastly expand the range of physiological phenomena accessible to monitoring.

Despite the significance of electromagnetic signal sources in biomedicine, tools for measuring electric, magnetic, and photonic events in tissue are limited. Macroscopic fields arising from gross muscle contraction and synchronized neural activity can be measured using techniques like electromyography, electroencephalography, and magnetoencephalography[1, 7], but these methods are very poor at localizing signal origins and cannot discern events at cellular or near-cellular scale. Probes based on glass micropipettes and metal electrodes can be used to record electrical events at a single cell level from neurons and cardiomyocytes in freely moving animals, but require invasive and technically difficult spatial targeting[18, 19]. Microfabricated arrays of electrodes provide multiplexed recordings of extracellular electrical signals from tens or hundreds of locations in human subjects[20, 21], but also target relatively few points in space and commonly require invasive, wired connectivity. Although minimally-invasive optical technologies are available for wide-field high-resolution neurophysiological recordings through thinned skull in rodents[22, 23], these methods are not easily translatable to primates and cannot reliably measure signals

below about 1 mm depth. These limitations, coupled with the danger of chronic and acute adverse reactions to both electrical and optical wired probes, highlight the need for minimally invasive approaches to the detection of biomedically-relevant electromagnetic fields in opaque tissue.

Probe technologies that interact with noninvasive imaging modalities offer an enticing alternative to more traditional approaches for tetherless detection of electromagnetic fields in biological systems. By converting fields at their sites of origin to changes in localized imaging signals, such probes can avoid the need for powered transmission of information out of the tissue. One demonstration of this type of strategy employed piezoelectric microcircuits to sense neural activity by converting bioelectric events to ultrasonic waves detectable by a remote transducer[24, 25]. To overcome the attenuation of ultrasound by bone, brain applications may rely on a subdural receiver to amplify the deep tissue signals and convert them to radiofrequency (RF) signals for recording outside the body[24]. Molecular probes suitable for magnetic resonance imaging (MRI)-mediated detection of electromagnetic events have also been introduced. They exploit the superior depth penetration and robustness of MRI-based detection methods. *In vitro* studies have reported detection of electric field fluctuations using a hydrogel-based MRI contrast agent[26], as well as photon detection using light-sensitive imaging agents[27, 28]. An important goal in adapting MRI-based probes for *in vivo* use is to improve their sensitivity to biologically-relevant electromagnetic stimuli. In this regard, a microfabricated imaging agent that uses circuit-based amplification mechanisms to convert biophysical signals into MRI-detectable magnetic or RF signatures could constitute an attractive strategy for measuring electromagnetic events in living subjects.

To implement such an approach, we here introduce the concept of *imp*lantable *a*ctive *c*oil-based *t*ransducers (ImpACTs), designed for wireless reporting of optical and electrical events in deep tissue, without the need for onboard power, in conjunction with MRI-based detection and localization. ImpACTs are millimeter or submillimeter-scale implantable devices that function like miniaturized variants of a standard circuit (RF coil) that stimulates and detects MRI signals from a subject. In response to biological electromagnetic stimuli such as voltage or photonic input, the coils become actively tuned or detuned, changing their resonance characteristics and therefore their ability to couple inductively to the main MRI detection hardware, a large RF antenna that either sits over an area of interest (surface coil) or around the subject (volume coil). The strength of coupling between each ImpACT and the main coil, along with the duration and strength of RF impulses applied to the main coil, determines how bright the local MRI signal near the ImpACT will appear in an image, and therefore provides the basis for an MRI-based readout of localized biophysical signals.

The ImpACT devices are fabricated as modified thin-film inductor-capacitor circuits. Tuning changes are actuated by altering the gate-source voltage (V_{GS}) across a field-effect transistor (FET) placed in parallel with the other circuit elements (**Fig. 1**). Changes to V_{GS} close or open the FET, shunting current to or from the coil's inductor and capacitor and altering performance of the circuit. In this context, the ImpACT gate electrode acts as a sensor, and can be rendered responsive to almost any electromagnetic signal of interest, relying on the same principles of commonly used, tethered FET-based biosensors that can sense electrophysiological activity[29, 30], light[31, 32], and biochemical analytes[33-35]. In each case, the inductor element of the circuit can be used to harvest the RF energy needed to produce a sufficiently large drain-source voltage (V_{DS}) for the device to be in open mode

without any bias voltage. We reasoned that such architectures could therefore provide a versatile basis for rapid detection of a variety of physiological events by MRI.

RESULTS

Theoretical characteristics of ImpACT devices

To explore the potential of ImpACTs to sense biologically-relevant signals, we began by modeling their predicted responses to realistic biophysical signal sources. Biophysical potentials range from tens to hundreds of microvolts in the case of neuronal extracellular field potentials, and reach tens of millivolts in the case of muscle contraction, cardiac activity, neuromuscular synaptic events, and oscillations in the central nervous system[21]. Meanwhile, photonic signals generated by luminescent cell lines and animal models attain flux values of 10^{10} photons per second (p/s) or more, depending on which luminescent reporter is used and on the factors regulating its activity[17, 36, 37]. To test the prospects for detecting such signals, we simulated the response of the devices as a function of three key parameters: (1) the input signal introduced at the FET gate electrode, simulated as a change in the source-drain conductance of the FET due to alteration of its gate-source voltage (V_{GS}) or to photonic input when using a photosensitive FET (photoFET); (2) the diameter of the ImpACT device's inductor (d), which determines its overall size; and (3) the thickness of the metal film (t_m) used in the device's circuitry.

The simulation model consisted of a circuit equivalent to the ImpACT device inductively coupled to a circuit representing a typical transmit-receive MRI volume coil (**Fig. 2a**). The ImpACT frequency response is measured as a tuning curve—the graph of the RF signal reflected from the main MRI RF coil, versus transmission frequency (**Fig. 2b**). The

minimum of the curve indicates the ImpACT's tuning frequency ν, and the ratio of this frequency to the full width at half height of the curve is the device's quality factor Q. The ImpACT transmits greatest power when its Q is maximized and its frequency matches that of the MRI RF transmit-receive coil. In our simulations, the ImpACT is initially tuned to the resonance frequency of $\nu = 400$ MHz, corresponding to an MRI operating magnetic field strength (B_0) of 9.4 T. Opening the FET or photoFET thus detunes the circuit. Response properties of these active elements were assumed to follow typical current-voltage characteristics, and were set according to specifications of sensitive commercially available FET devices used in our subsequent experiments. The source-drain resistance across the transistor falls from a value of 5 kΩ in the FET's closed state to a value of 0.2 kΩ in the FET's open state. Transitions between these values occur over an interval ranging between ΔV_{GS} = 0 to 500 mV, where ΔV_{GS} is the difference between V_{GS} and the threshold voltage for FET opening, V_{th}.

Fig. 2b illustrates the shift in tuning curve as a function of ΔV_{GS} for a representative simulation of an ImpACT with single-turn inductor diameter d = 10 mm and t_m = 10 μm. The tuned curve (low ΔV_{GS}) displayed Q of 17.7, while the detuned curve (high ΔV_{GS}) displayed a Q of 4.5. This corresponds to an input-dependent 8.6 dBV (2.7-fold) change in transmission efficiency through the ImpACT device.

Expected dynamic range and sensitivity in MRI

To predict how ImpACT tuning changes would be likely to affect actual MRI signals, we next used our simulation approach to estimate the strength of the local RF field induced in the ImpACT by the main coil in a realistic imaging scenario. The ratio of the ImpACT's

local field (B_{ImpACT}) to the field strength produced by the scanner's RF coil (B_1) provides an approximate measure of the local MRI signal amplification expected at the ImpACT location (see Methods for details).

Fig. 2c depicts B_{ImpACT}/B_1 as a function of voltage or photonic input amplitude for ImpACT devices with a range of diameters and t_m = 10 μm. For ImpACTs with d = 1, 3, and 5 mm at zero input, values of B_{ImpACT}/B_1 are 1.2, 1.8, and 3.6, respectively; with 500 mV (10^{11} p/s) input B_{ImpACT}/B_1 values fall to 1.1, 1.3, and 1.1, reflecting a strong size dependence of device performance characteristics. These numbers correspond to stimulus-dependent modulation by up to 70% for the largest devices across the full range of input strengths we examined (**Supplementary Fig. 1**). For each ImpACT, changes in B_{ImpACT}/B_1 are approximately linearly proportional to inputs in the 0–300 mV range, also equivalent to luminescent inputs of 0–1.7 x 10^{10} p/s falling on the 0.09 mm^2 photoFET light sensor we modeled. For inputs greater than 300 mV or 1.7 x 10^{10} p/s, the predicted ImpACT responses become increasingly nonlinear; they reach an asymptote by input levels of 500 mV or 10^{11} p/s, at which point the FET or photoFET component is fully open and the ImpACT cannot be further detuned. These input levels thus establish an upper bound on the dynamic range of the devices.

To estimate ImpACT responses to small biological-scale inputs, we predicted the modulations in B_{ImpACT}/B_1 expected to arise from inputs of 10 mV or 2 x 10^9 p/s, compared with zero input (**Fig. 2d**). For ImpACTs with d = 0–3 mm, the modeled signal change varies linearly in proportion to device size; above d = 3 mm, sensitivity to 10 mV inputs reaches a plateau, with expected modulations of about 1.6% in B_{ImpACT}/B_1. We also esti-

mated the minimum detectable ImpACT input, operationally defined as the voltage or photonic amplitude required to produce a 1% change in B_{ImpACT}/B_1 from its base value (**Fig. 2e**); this definition justified by the fact that functional MRI experiments commonly detect imaging signal changes of about this magnitude or larger. Based on this criterion, we predicted that a 5 mm single-turn ImpACT could sense inputs as low as 5.4 mV, comparable to extracellular electrical potentials, and that a 1 mm device could sense inputs of at least 20.8 mV, comparable to transmembrane voltages in single cells. Devices of d = 1 mm and 5 mm could also detect photonic inputs of 4.2 x 10^9 p/s and 1.1 x 10^9 p/s, respectively. With changes to the metal layer thickness, FET transconductance, and number of turns, additional sensitivity improvements or reductions in device dimensions could be possible; sensitivity to inputs below 10 mV are predicted for multi-turn ImpACTs as small as 250 μm in diameter (see **Supplementary text** and **Supplementary Figs. 2-4**).

Validation of ImpACTs in MRI

In order to validate our simulations and verify the ability of an actual ImpACT to undergo stimulus-dependent changes in tuning in an experimental setting, we constructed a series of single-turn thin film FET-gated circuits. A device with d = 3 mm and t_m = 10 μm is depicted in **Fig. 3a** and diagrammed in **Fig. 3b**. A second ImpACT with dimensions matching the model parameters of **Fig. 2b** (d = 10 mm) was used for experimental validation of the predicted tuning behavior. Using a network analyzer inductively coupled to the device, we measured the frequency response over a range of ΔV_{GS} values (**Fig. 3c**). Behavior of this ImpACT closely paralleled the simulated results, with Q values of 17.9 and 4.5

in the fully tuned and detuned states, respectively, almost exactly matching the model calculations. To probe the sensitivity of the device, we then examined the ImpACT's response to the millivolt-scale inputs most relevant to biophysical phenomena. Inputs with ΔV_{GS} = 0–90 mV in 10 mV increments all produced discernible changes in the ImpACT tuning curve (**Fig. 3d**). The responses are equivalent to an average change in reflected amplitude by 0.61 ± 0.11 dBV per 10 mV input increment, indicating that millivolt-scale inputs are easily detectable.

The performance characteristics indicated by the tuning curves of **Fig. 3c-d** apply to behavior of ImpACT devices during steady-state RF irradiation, but imaging applications would require the ImpACT to be functional during highly transient RF pulses typical of MRI scanner operation. In order to test the ImpACT device's functionality and sensitivity in imaging, we performed MRI of FET and photoFET-based ImpACT devices during modulation of their voltage or photonic input. The devices were placed inside a 78 mm diameter MRI transmit-receive coil while a simple MRI gradient echo pulse sequence with excitation pulse width of 1 ms and flip angle 30° was applied. Parallel changes in tuning and image intensity could be obtained across wide dynamic ranges, using both types of input (**Supplementary Fig. 5**). Representative results obtained using a photo-sensitive ImpACT constructed with d = 3 mm and t_m = 10 μm are shown in **Fig. 3e**. The device was tuned to the MRI scanner's operating frequency of 400 MHz in the absence of input; in this condition, the MRI signal proximal to the inductor element of the circuit was 30.4 ± 4.7% higher than the water signal distal to the device, reflecting local intensification of RF flux by the ImpACT in its tuned state. When an input of 1 x 10^{11} p/s was applied, the MRI signal

enhancement near the ImpACT diminished to only 5.6 ± 2.7% over baseline, a significant input-dependent decrease (*t*-test $p < 0.005$ over the $n = 8$ closest image pixels).

To examine the likely specificity ImpACT-mediated MRI signal to input-dependent modulations, we examined the ImpACT's sensitivity to the extraneous environmental factors that could vary in realistic contexts. In order to quantify the effect of ion concentration in the vicinity of the 3 mm ImpACT, we performed measurements over a range of buffer dilutions (**Supplementary Fig. 6a**). The results indicate that at salt concentrations relevant to serum or cerebrospinal fluid (150 mM and above) ImpACT tuning varies by only 0.05% per millimolar, meaning that dramatic fluctuations of over 10 mM in ionic strength would be required to produce MRI changes comparable to those elicited by even the smallest detectable voltage or photonic inputs. Similarly, ImpACT responses to temperature variation were minimal. Even across an unphysiologically large range of temperatures from ~22 °C to 37 °C, the experimentally determined tuning characteristics as a function of input are barely affected (**Supplementary Fig. 6b**). The MRI scanner's B_0 field is another environmental parameter that can vary somewhat, typically on the order of 10 parts per million[38], due primarily to spatial variations in magnetic susceptibility in tissue. To model such effects, we examined the ImpACT's response to tuning offsets by up to 1 MHz from the main B_0 resonance frequency and showed that under all conditions the tuning behavior as a function of input remains approximately unchanged (**Supplementary Fig. 6c**). Local B_1 fields produced by the scanner's main coil can also vary somewhat in realistic scanning conditions. Such inhomogeneities are not expected to affect the interpretability of ImpACT-mediated responses, however, because the ImpACT's signal enhancement simply scales with

whatever the local B_1 is (see **Fig. 2** and **Supplementary Figs. 1-2**). Differences in the angular orientation of an ImpACT could affect inductive coupling to the main coil and thus alter the magnitude of signal enhancements, but even these would not affect the profile of relative ImpACT responses to inputs of varying amplitude.

Performance of ImpACTs in clinically-relevant settings

Initial assessment of our ImpACT devices was performed at a field strength of 9.4 T, but potential clinical applications would likely involve considerably lower B_0 fields. To test ImpACT performance at a clinically relevant magnetic field strength, we constructed a 3 mm ImpACTs tuned for operation in a 3 T MRI scanner and compared its performance with results obtained at 9.4 T (**Supplementary Fig. 7**). The experimental dynamic range is similar at both field strengths, although the ImpACT response reaches an asymptote at somewhat lower input strength at lower field (400 mV *vs.* 500 mV). Modeled performance of ImpACT devices as a function of field strength (**Supplementary Fig. 7c**) shows that the minimum detectable signal also increases at lower field. At 3 T, an ImpACT with d = 3 mm and t_m = 10 μm is predicted to detect 14.6 mV or 2.9 x 10^9 p/s inputs, whereas a similar device tuned to operate at 9.4 T could detect somewhat weaker inputs of 6.4 mV or 1.3 x 10^9 p/s.

A limitation on the application of some implantable electronic devices in biomedical settings is the propensity of such devices to deposit energy into biological tissue, leading to local heating and potential damage. The amount of energy deposition depends on an interaction among multiple device- and tissue-dependent factors that together determine the specific absorption rate (SAR). A simple upper bound on the SAR for an ImpACT

device can be calculated by determining the total power dissipated in the ImpACT itself and normalizing this by the tissue volume likely to be affected by each individual device, here approximated as a sphere equal to twice the device diameter. To compute this quantity, we used our simulation approach to determine the peak instantaneous power deposition, assuming operation at 400 MHz with a typical main coil RF field strength (B_1 = 2 μT). We found that upper bounds on SAR ranged from 8 x 10^{-3} W/kg for a 1 mm device to 3 x 10^{-4} W/kg for a 5 mm device (**Supplementary Fig. 8**). Using a 3 mm ImpACT operated continuously for two hours with a pulse sequence repetition time of 2 s in contact with a 1 mL buffer sample, we found that mean temperature rose by at most ~1 °C, indicating a combined power deposition from the main B_1 coil and the ImpACT of less than 6 x 10^{-4} W across the specimen. Such values fall well within safety margins of several W/kg specified by the US Food and Drug Administration[39], and indicate that ImpACT devices will be safe for use in animals and people.

ImpACT-based detection of bioluminescence *in vitro* and *in vivo*

To examine performance of an ImpACT device in biological settings, we attempted to modulate ImpACT-mediated MRI signals using biogenic sources. We chose to focus initially on bioluminescent detection (**Fig. 4a**) because this modality does not require electrical contact between the sensor and the specimen being measured. Using the photosensitive ImpACT device with d = 3 mm, we began by examining MRI signal when the device was stimulated by a 7.8 μM luciferase solution, following addition of 1 mM D-luciferin and 1 mM adenosine triphosphate (ATP). The enzymatic reaction generated sufficient light flux to detune the device, producing an MRI signal decrease of 16 ± 7%, with respect to

the signal observed in the absence of luciferase (**Fig. 4b**). Minimal MRI signal changes of only 0.4 ± 5.4 % were measured in the presence of luciferase, but without luciferin or ATP. Using network analyzer measurements, we verified that the luciferase-mediated response in **Fig. 4b** was caused by detuning of the ImpACT; luciferase activity decreased the device's *Q* value by 3.8 ± 0.8% and induced a tuning frequency shift of 2.7 MHz (**Fig. 4c**).

These measurements demonstrate the ability of the ImpACT design to transduce bioluminescence signals to an MRI detectable signal change. We next sought to determine whether endogenously expressed luciferase inside cells could produce similar effects. HEK293 cells expressing an engineered luciferase (NanoLuc) were placed in proximity to the 3 mm ImpACT. Upon addition of the luciferin analog furimazine, a 3.6 ± 0.6% decrease in MRI signal that persisted for more than 60 minutes was observed (**Supplementary Fig. 9**). No signal change was observed distally from the device.

Cellular expression of luciferase is widely used *in vivo* as a reporter for cell density and status in animal models of tumorigenesis and transplantation; we therefore asked whether an ImpACT could reveal the presence of luciferase-expressing cells in a living animal. NanoLuc-expressing HEK293 cells were xenografted into the cerebral cortex of anesthetized rats, and 3 mm ImpACT devices were implanted over the cells (**Fig. 4d-e**). MRI scanning was performed before, during, and after intracranial injection of 1 mM furimazine substrate (3 μL) proximal to the cell implantation sites. During injection and spreading of the furimazine in the brain parenchyma, we observed a significant average signal decrease of up to 16.2 ± 2.3% (*t*-test $p = 0.006$, $n = 4$) that developed and persisted for over 80 minutes (**Fig. 4f-g**), consistent with infiltration of furimazine into the NanoLuc-expressing cell implants and subsequent stimulation of the photosensitive ImpACTs. This

mean signal change was 4.5 times the amplitude produced by 10^4 cells/μL in the *in vitro* experiment of **Supplementary Fig. 9**, and therefore suggests that the MRI signal change observed *in vivo* arose from approximately 5 x 10^4 cells/μL in the sensitive area of the ImpACT.

The MRI change produced by the ImpACT in the vicinity of bioluminescent cells and furimazine injection was significantly different from variations of the MRI signal distal to the ImpACT probes (paired *t*-test $p = 0.02$, $n = 4$), demonstrating that the devices themselves mediated the observed signal changes. MRI scans performed after the experiments showed no evidence of tissue disruption. Furthermore, when the experiments of Fig. 4f-g were repeated with control injections of a fluid lacking furimazine, a statistically insignificant mean MRI intensity increase of 0.4 ± 1.3% was observed (*t*-test $p = 0.8$, $n = 3$; **Supplementary Fig. 10**). In addition to verifying that the signals documented in **Fig. 4f-g** arise from bioluminescence detection by the ImpACT devices, the absence of MRI changes in the vehicle control time courses shows that ImpACT devices can perform stably, without clearly discernable signal drift or biotoxicity, for periods of over two hours *in vivo*.

In the experiments of **Fig. 4d-g**, ImpACT responses to bioluminescent cells in rat brain are slow and monotonic, likely reflecting the combination of diffusive spreading of the furimazine substrate from its infusion site, and the relatively constant metabolism of furimazine by NanoLuc-expressing cells. Such time courses are qualitatively consistent with bioluminescence time courses previously observed *in vivo*[40], but do not indicate intrinsic temporal limitations of the ImpACT itself. To assess the device's ability to function on a much faster time scale, we stimulated an implanted device directly with a fiber optic light source and monitored its response characteristics *in vivo* (**Supplementary Fig. 11**).

Repeated cycles of light delivery and rest show that the device rapidly cycles between tuned and detuned states with no apparent hysteresis on the time scale of the scan duration. The results also provided an additional testament to the stable performance of ImpACTs *in vivo*, with no observable attenuation of the light-dependent responses over the 20 min acquisition time investigated. An average MRI signal decrease of 12.7 ± 0.7% was observed, with a coefficient of variation of ~10% denoting reproducible performance over four stimulation blocks. These measurements therefore collectively demonstrate that ImpACT devices can detect biologically relevant electromagnetic fields reversibly and over a range of time scales in living animals.

DISCUSSION

Our results demonstrate a new principle for minimally invasive detection of biological signals using biosensitive implantable microdevices that produce localized image changes in MRI. The ImpACT devices accomplish this using simple resonant circuits that require no external power and are detuned by input to a FET. ImpACTs offer several advantages with respect to other implantable device technologies: they are unwired and interact only passively with detection hardware, they do not need to transmit signals out of the body, and they can readily be spatially multiplexed in scalable fashion, in conjunction with MRI-based localization. The ImpACT design closely parallels that of detunable surface coils for MRI, but on a miniature scale and using components sensitive to biologically realistic inputs. In this work we have shown detectability of voltage signals as low as 5.3 mV and luminescent input as low as 1 x 10^9 p/s. A light sensitive ImpACT was tested *in vivo* and successfully monitored the output of a luciferase gene reporter expressed in a

tumor cell model. This was achieved in conjunction with standard MRI hardware, without danger of excessive local energy deposition.

The millimeter-scale devices used in this study could be deployed in many organs of the body where external monitoring of electromagnetic fields is desired. The ImpACT we used for our *in vivo* experiments in particular had a 3 mm diameter, comparable to some electronic implant designs that function by different principles[41]. A goal for future development will be to further miniaturize the devices in order to permit placement using endoscopic procedures, or perhaps even infusion into the vasculature. Our theoretical calculations provide a basis for such efforts, showing that ImpACTs with submillimeter diameters are feasible using multiturn designs (**Supplementary Fig. 4**). The t_m values of several microns required for optimum functionality of such devices can easily be achieved with electroplating techniques used for microfabricated tethered MRI diagnostics devices[42, 43]. Some studies have demonstrated high performance microscale coils using wire bonding[44, 45], but this limits scalability due to the serial fabrication process involved. Our design, by contrast, employs processes that are easy to implement in parallel, providing a route for mass production with low manufacturing costs.

Another goal for future development of ImpACT technology is to expand the scope of potential applications *in vivo*. For chronic applications in animals or people, this will involve ensuring that the devices are stable and biocompatible over long periods of time. The presented results already demonstrate consistent MRI signal in proximity to ImpACTs over periods of several hours (**Supplementary Fig. 10**), as well as reproducible, repeated responses to equivalent stimuli across multiple animals (**Fig. 4**) and multiple cycles of stimulation (**Supplementary Fig. 11**). Further applications may benefit in addition from

passivation strategies that promote tissue compatibility and effective performance of the devices over days, months, or years[46]. Expanding the scope of utility may also involve exploring how ImpACT devices could be used in conjunction with diverse magnetic resonance hardware. Although we have shown compatibility of the ImpACTs with MRI-based detection in both conventional clinical and small-bore scanners, multiplexed detection of ImpACTs could be possible using portable systems[47-49], albeit with some loss of sensitivity at lower B_0 field (**Supplementary Fig. 7**).

When combined with any suitable detection hardware, the ImpACTs we have validated here could be used to detect luminescent reporter gene expression in applications such as following tumor growth and treatment in animal models, studying lymphatic function mediated by engineered immune cells, or monitoring luciferase-expressing transplanted cells and tissues, potentially in human subjects[16, 50]. For each of these applications, the current light sensitivity of ~1 x 10^9 p/s, should permit imaging of cellular events involving expression of 10^5-10^6 copies of luciferase per cell, assuming enzyme turnover number ranging between 0.1 and 1 s^{-1}, with as few as 10^4–10^5 cells in the vicinity of the 300 x 300 μm light sensitive area of the current device. Integrating ImpACTs with low dark current photodiodes would require additional components for more efficient RF power harvesting by the circuit, but could permit detection of as little as 10^6 p/s, enabling sensitivity to luminescent events involving more than an order of magnitude fewer cells or luciferin turnover events. These might for instance enable dynamic activity monitoring of calcium-sensitive bioluminescent probes such as aequorin[51], estimated to generate fluxes of 1.3 x 10^3 p/s per neuron when expressed in vertebrate brains.

The voltage-dependent ImpACT characterized in **Fig. 3** displays sensitivity to inputs of 5 mV or more in MRI experiments *in vitro*, and could also be applied for wireless measurements in more or less its present form. The device's sensitivity is sufficient in principle for dynamic detection of long-range extracellular potentials arising from activated cell populations in neural and muscle tissue. If the device is placed in close apposition to single cells[52-55], even individual action potentials could be detectable. Detection of millisecond-timescale transient electrophysiological events is possible provided that those events produce input to the ImpACT during application of the MRI pulse. As such, the short duration of intracellular and extracellular potentials in electrically active tissue does not present a challenge to their detection using ImpACT technology. Improved sensitivity for detection of single cell electrical potentials could be achieved by optimizing FET current-voltage characteristics for more robust detuning of the devices, potentially using nanowire-based FETs that have been applied in the past for wired electrophysiology measurements[21].

Another exciting avenue for further development will be the sensitization of ImpACT devices to chemical signals, which can be performed via functionalization of the gate electrode of ion-sensitive FETs with biochemically active agents such as enzymes and antibodies[33, 35, 56]. This would enable ImpACT-based detection of diverse analytes with high specificity, in proportion to their concentration, via enzymatic or biochemical recognition events that alter transconductance of the FET. Along with further applications to detection of electromagnetic fields, the possibility of chemical detection using ImpACTs highlights the versatility of this family of devices for dynamic functional imaging that leverages the spatiotemporal resolution and whole-body volumetric readout capabilities of MRI.

Author contributions

AH and AJ devised the ImpACT concept. AH, VCS, BBB, and AJ designed the research. AH performed modeling calculations. AH and VCS performed the *in vitro* measurements and analyzed the data. AH and BBB performed *in vivo* imaging experiments. AH and AJ wrote the manuscript.

Competing interests

MIT has filed a provisional patent application related to this technology.

Additional information

Correspondence and requests for materials should be addressed to AJ.

Acknowledgements

This research was funded by NIH grants R01 NS76462, R01 DA038642, and U01 NS904051 to AJ. AH was supported by postdoctoral fellowships from the Edmond & Lily Safra Center for Brain Sciences and a long-term fellowship of the European Molecular Biology Organization. We thank Atsushi Takahashi for assistance with 3 T MRI measurements.

METHODS

ImpACT simulations

Performance of ImpACT devices was simulated using equivalent circuit models implemented in PSpice (Cadence Design Systems, Chelmsford, MA). The MRI scanner's

transmit-receive coil was represented by a resistor-inductor-capacitor (RLC) circuit, assuming a 78 mm diameter (L = 143.3 nH), 50 Ohm impedance and a sinusoidal voltage source as coil output. The main coil was inductively coupled to the ImpACT (coupling coefficient k = 0.00275-0.275), which was represented by another RLC circuit, connected in parallel to a FET component. The ImpACT inductance ranged from 0.2 to 32 nH, and the capacitance ranged from 4.8 to 791.7 pF. The resistance was calculated based on sheet resistance considerations and skin depth at 400 MHz. Sensitivity profiles of the modeled FET devices simulated here were obtained with reference to published characteristics of 2N5486 MOSFET from Central Semiconductor Corp. (Hauppauge, NY) and the SFH3310 photoFET from Osram Opto Semiconductors (Regensburg, Germany), respectively.

Current output from the model was converted to magnetic field near the ImpACT device (B_{ImpACT}) by using the Biot-Savart law for magnetic field produced by a current loop, and the ratio between B_{ImpACT} and the B_1 of the main coil was used as an estimate of MRI signal amplification due to the device. Justification for this approach is that for a wide family of MRI pulse protocols, including the gradient echo methods used in this paper, the MRI signal amplitude detected is proportional to $\sin(\alpha)$, where α is the flip angle of the excitation pulse. Since α is in turn directly proportional to the local RF field during the excitation pulse, the local amplification of this field (as reflected by B_{ImpACT}/B_1) will also determine the local amplification of MRI signal. This analysis applies to low flip angles, significantly less than 90°, as typically used in longitudinal relaxation time (T_1)-weighted imaging. For larger flip angles, the relationship between local B_1 enhancement and resulting MRI signal will be more complex, but may nevertheless be analytically derived. Note

that this analysis ignores the potential effect of ImpACT detuning on signal reception during the acquisition phase of the MRI pulse sequence; this effect is harder to model, but if present, would synergize with effects due to ImpACT tuning during pulse generation. For the two-dimensional plots of **Fig. 2** and **Supplementary Figs. 1-2**, we evaluated 55 input values between 0 and 500 mV (0 and 10^{10} p/s) spaced linearly according to the equivalent FET channel conductivity, 18 diameter values spaced logarithmically between 10 and 5000 μm, and 10 t_m values spaced linearly between 1 and 10 μm. $\Delta(B_{\mathrm{ImpACT}}/B_1)$ values presented in **Supplementary Figs. 1-2** were determined as the B_{ImpACT}/B_1 for the parameters indicated by the axes minus the B_{ImpACT}/B_1 for zero input.

Calculation of power dissipation

We estimated an upper bound on the maximum local specific absorbance rate (SAR) of an ImpACT by calculating the maximum instantaneous power (P) deposited in the ImpACT during an RF pulse and normalizing this by a spherical volume of tissue (V) around the device, with twice the diameter of the device (d). This volume was chosen conservatively to reflect the maximal density at which multiple functional ImpACT devices could be spaced in tissue, with a separation of twice their diameter minimizing the potential for electromagnetic coupling between the devices; in most applications, the inter-device spacing and corresponding volumes of power dissipation are likely to be much greater. Under the simulation conditions, we calculate:

$$\frac{P}{V} = \frac{\rho I_{\mathrm{ImpACT}}^2 R_{\mathrm{ImpACT}}}{4/3 \pi d^3} \qquad (1)$$

where ρ is the tissue density (approximately 1 kg/L), R_{ImpACT} is the device impedance at 400 MHz, and I_{ImpACT} is the current induced in the device, computed using the B_{ImpACT}/B_1

ratios of **Fig. 2c** and assuming an applied RF field of 2 μT. The value of 2 μT for the scanner's RF pulse amplitude is chosen by assuming a pulse width (t_p) of 1 ms and a flip angle (α) of 30°, using the formula:

$$B_1 = \frac{\alpha}{\gamma t_p} \qquad (2)$$

with proton gyromagnetic ratio γ of 42.6 MHz/T. The P/V values computed using Eq. 1 and presented in **Supplementary Fig. 5** are likely to be substantial overestimates of the actual SAR, for three reasons: (1) because of the sparse duty cycle of pulsing in a typical MRI experiment (usually less than 1%); (2) because only a fraction of the power dissipated in the ImpACT is actually likely to be transferred into the tissue as heat; and (3) as noted above, because the tissue volume over which power can be spread will likely be significantly greater than twice the device diameter.

Device fabrication and characterization

Circuits were fabricated using standard printed-circuit single turn inductors with 10 μm gold-plated copper as conductive layer. Coil radius ranged from 500 μm to 5 mm with line width of 0.1–1 mm. Coils were soldered to trimmer capacitors with adjustable capacitance of 5.5–30 pF (Knowles Voltronics #JR300, Cazenovia, NY). For voltage measurements, we used N-Channel 400 MHz RF MOSFETs with internal capacitance of 5 pF (Central Semiconductor Corp. #2N5486). For MRI photodetection and bioluminescence measurements we used NPN phototransistors with 570 nm wavelength peak sensitivity and collector emitter capacitance of 2.2–4.0 pF (Osram Opto Semiconductors #SFH3310). The photon-sensitive area of these components was 300 x 300 μm. For bioluminescence measurements outside of the MRI scanner, we used the IVIS Spectrum *In Vivo* Imaging System

(PerkinElmer #124262, Waltham, MA). Current measurements were made using a custom-made amperometer circuit and 10 GHz oscilloscope (Keysight Technologies #DSO81004B, Santa Rose, CA). Resonance frequency characterization was performed using RF network analyzer (Keysight Technologies, #E5061A) by way of reflected amplitude measurements using a loop antenna comprised of 2 mm copper-shielded coaxial silver wire (Pasternack #RG402-U, Irvine, CA), placed 0.5 mm above the ImpACT inductor. For water phantom measurements, 0.5 mL microcentrifuge tubes were cut and cured on top of the ImpACT coils using epoxy glue. Temperature measurements were performed using SurgiVET Advisor monitor and V3417 temperature probe (Smiths Medical, Norwell, MA).

Magnetic resonance imaging validation and data analysis

Magnetic resonance imaging was performed primarily using a 9.4 T Avance II MRI scanner (Bruker Instruments, Ettlingen, Germany). Additional measurements at clinical field were performed using a Siemens (Erlangen, Germany) 3 T MAGNETOM Tim Trio scanner. ImpACT devices were cured to polymer tubes for measurement in solution, and placed within a birdcage transmit-receive imaging volume coil (inner diameter 78 mm). Response to light intensity was done in light tight chambers. Both T_1-weighted scans and transverse relaxation time (T_2)-weighted scans with 0.1–1 mm slice thickness across the surface of the devices were acquired using gradient echo and fast spin echo pulse sequences. Echo time (*TE*) of 15.6 ms and repetition times (*TR*) of 250 and 787 ms were used. Data matrices of 64 x 64, 128 x 128, and 256 x 256 points were taken, with 1–10 averages, and total scan time ranging between 16 seconds and 10 minutes. Intensity values

in square regions of interest at the center of the device surface were determined from reconstructed magnitude images and compared with baseline values from regions distal to device. Analysis was performed using custom routines written in MATLAB. Time lapse scans for functional imaging were obtained using a gradient echo pulse sequence with a flip angle of 30°, *TR* of 236 ms, *TE* of 15.6 ms, field of view (FOV) of 25.6 x 25.6 mm, data matrix of 128 x 128 points, and 1 mm coronal slice thickness, with 16 s scan time. Scans were obtained consecutively for 60 minutes. Post-processing of MRI data was performed using customized routines in MATLAB (Mathworks, Natick, MA). Raw images were analyzed per region of interest around inductor element of device for the quantification of signal amplitude before and after detuning.

Cellular expression of luciferase

Phantom measurements were taken using either dionized water or phosphate buffer saline, at pH 7.4, at room temperature. Magnetic resonance imaging of biological luminescence was performed in phosphate buffered saline, using recombinant luciferase from *Photinus pyralis* (Sigma Aldrich, #SRE0045, Natick, MA) at a concentration of 7.8 μM and initial volume of 100 μL. D-luciferin (Sigma Aldrich, #L9504), at concentration of 7.8 mM in argon-bubbled dionized water and equimolar concentration of sodium bicarbonate, and adenosine 5′-triphosphate (ATP) disodium salt hydrate (Sigma Aldrich, Cat# A2383) at a concentration of 7.8 mM, were each dissolved at a volume of 50 μL and were both mixed with luciferase solution during MRI to achieve working concentration of 3.9 μM of luciferase, and 3.9 mM of luciferin and ATP. For bioluminescence cell measurements we used a HEK293 cell line transfected with NanoLuc engineered luciferase plasmid (Promega

#N1441, Madison, WI). Bioluminescence was measured 48 hours after transfection by adding 1–5 mM furimazine (Promega, #N205A) to 10 million cells per mL in Tris buffer at the phototransistor component of device.

Animal use

Male Sprague-Dawley rats (250–300 g) were purchased from Charles River Laboratories (Wilmington, MA) and used for all *in vivo* experiments. Animals were housed and maintained on a 12 hr light/dark cycle and permitted *ad libitum* access to food and water. All procedures were performed in strict compliance with US Federal guidelines, with oversight by the MIT Committee on Animal Care.

MRI detection of luciferase-expressing cells *in vivo*

Intracerebral guide cannulae were implanted surgically to facilitate intracranial injection of furimazine in MRI experiments, emulating previously described methods[57]. Animals were anesthetized with isoflurane (4% induction, 2% maintenance), shaved, and mounted on a rodent stereotaxic device (Kopf Instruments, Tujunga, CA) with heating pad. Heart rate and blood oxygenation were continuously monitored using a pulse oximeter (Nonin Medical, Plymouth, MN) during all subsequent procedures. The scalp was retracted and two small holes were drilled into the skull, 7 mm and 9 mm posterior to bregma and 0.5 lateral to the midline. An MRI-compatible 2 mm-long guide cannula (22 gauge; PlasticsOne, Roanoke, VA) was implanted at the anterior site. 10 µL of NanoLuc-expressing HEK293 cell slurry (containing ~5 million cells) was injected into the cortex at the posterior site, and an ImpACT device was implanted over the cells. A custom fabricated plastic

headpost was attached to the skull in front of the guide cannula, and dental cement was applied to secure all implants rigidly in place. Buprenorphin (0.05 mg/kg) was injected subcutaneously during surgery. An MRI-compatible injection cannula (3 mm long below pedestal, PlasticsOne) was connected to microtubing pre-filled with 5 µL 7.8 µM furimazine. The injection cannula was slowly lowered into the previously implanted guide cannula while infusing furimazine at a small injection rate to prevent air from becoming trapped during insertion. The injection cannula was then secured to the guide cannula with dental cement, and the injection was paused.

Each animal was then transferred to a plexiglass cradle covered with a water heating blanket to maintain body temperature, and inserted into a transmit-receive volume coil (Bruker Instruments, Billerica, MA). The animal was positioned at the isocenter of a 9.4 T Bruker Avance II scanner (Bruker Instruments). Heart rate and oxygen saturation levels were monitored throughout the scan using Nonin 8600V pulse oximeter (Nonin Medical, Plymouth, MN), and breathing and expired CO_2 were monitored using a SurgiVet V9004 Capnograph (Waukesha, WI). Heart rate was maintained at 360–380 bpm. Animals were maintained with continuous delivery of 1.5% isoflurane for the duration of the scanning sessions.

For *in vivo* MRI analysis, T_1-weighted scan series and T_2-weighted anatomical scans were obtained from each animal. Multislice anatomical images with 200 µm in-plane resolution over six 1 mm sagittal slices were obtained using a rapid acquisition with relaxation enhancement (RARE) pulse sequence with a *TR* of 2 sec, *TE* of 14 ms, RARE factor of 8, field of view of 25.6 x 25.6 mm, data matrix of 128 x 128 points, 4 averages and a total scan time of 80 sec. Scan series for functional imaging were obtained using a gradient echo

pulse sequence with a flip angle of 30°, *TR* of 126 ms, *TE* of 10 ms, FOV of 25.6 x 25.6 mm, data matrix of 128 x 128 points, and 1 mm sagittal slice thickness, with 16 s scan time per image. Scans were obtained consecutively for 120 minutes; from t = 5 to 35 minutes, furimazine was infused at a constant rate of 0.1 μL/min.

Reporting Summary

Further information on experimental design is available in the Nature Research Reporting Summary linked to this article.

Code availability

The MATLAB code for simulation of MRI response and the design parameters of ImpACT devices is available from the corresponding author upon reasonable request.

Data availability

The data that support the findings of this study are available within the paper and its Supplementary Information. All datasets generated for this study are available from the corresponding author upon reasonable request.

REFERENCES

1. Grosse, P., Cassidy, M.J. & Brown, P. EEG-EMG, MEG-EMG and EMG-EMG frequency analysis: physiological principles and clinical applications. *Clin Neurophysiol* **113**, 1523-1531 (2002).
2. Jasanoff, A. Bloodless FMRI. *Trends Neurosci* **30**, 603-610 (2007).

3. Logothetis, N.K. What we can do and what we cannot do with fMRI. *Nature* **453**, 869 (2008).

4. Bandettini, P.A. What's new in neuroimaging methods? *Ann N Y Acad Sci* **1156**, 260-293 (2009).

5. Regan, D. Human brain electrophysiology: evoked potentials and evoked magnetic fields in science and medicine. (Elsevier, New York; 1989).

6. Merletti, R. & Parker, P.A. Electromyography: physiology, engineering, and non-invasive applications, Vol. 11. (John Wiley & Sons, 2004).

7. Nunez, P.L. & Srinivasan, R. Electric fields of the brain: the neurophysics of EEG. (Oxford University Press, USA, 2006).

8. Bénar, C. et al. Quality of EEG in simultaneous EEG-fMRI for epilepsy. *Clin Neurophysiol* **114**, 569-580 (2003).

9. Pandarinath, C. et al. Neural population dynamics in human motor cortex during movements in people with ALS. *Elife* **4**, e07436 (2015).

10. Cash, S.S. & Hochberg, L.R. The emergence of single neurons in clinical neurology. *Neuron* **86**, 79-91 (2015).

11. Wang, J. Amperometric biosensors for clinical and therapeutic drug monitoring: a review. *J Pharm Biomed Anal* **19**, 47-53 (1999).

12. Wang, J. Electrochemical biosensors: towards point-of-care cancer diagnostics. *Biosens Bioelectron* **21**, 1887-1892 (2006).

13. Sofic, E., Lange, K.W., Jellinger, K. & Riederer, P. Reduced and oxidized glutathione in the substantia nigra of patients with Parkinson's disease. *Neurosci Lett* **142**, 128-130 (1992).

14. Bergamini, M.F., Santos, A.L., Stradiotto, N.R. & Zanoni, M.V. A disposable electrochemical sensor for the rapid determination of levodopa. *J Pharm Biomed Anal* **39**, 54-59 (2005).

15. Wassum, K.M. et al. Silicon Wafer-Based Platinum Microelectrode Array Biosensor for Near Real-Time Measurement of Glutamate in Vivo. *Sensors (Basel)* **8**, 5023-5036 (2008).

16. Contag, C.H. & Bachmann, M.H. Advances in in vivo bioluminescence imaging of gene expression. *Annu Rev Biomed Eng* **4**, 235-260 (2002).

17. Weissleder, R. & Ntziachristos, V. Shedding light onto live molecular targets. *Nat Med* **9**, 123-128 (2003).

18. Lee, A.K., Manns, I.D., Sakmann, B. & Brecht, M. Whole-cell recordings in freely moving rats. *Neuron* **51**, 399-407 (2006).

19. Kodandaramaiah, S.B., Franzesi, G.T., Chow, B.Y., Boyden, E.S. & Forest, C.R. Automated whole-cell patch-clamp electrophysiology of neurons in vivo. *Nat Methods* **9**, 585-587 (2012).

20. Hochberg, L.R. et al. Neuronal ensemble control of prosthetic devices by a human with tetraplegia. *Nature* **442**, 164 (2006).

21. Spira, M.E. & Hai, A. Multi-electrode array technologies for neuroscience and cardiology. *Nat Nanotechnol* **8**, 83-94 (2013).

22. Stosiek, C., Garaschuk, O., Holthoff, K. & Konnerth, A. In vivo two-photon calcium imaging of neuronal networks. *Proc Natl Acad Sci U S A* **100**, 7319-7324 (2003).

23. Flusberg, B.A. et al. Fiber-optic fluorescence imaging. *Nat Methods* **2**, 941-950 (2005).

24. Seo, D., Carmena, J.M., Rabaey, J.M., Maharbiz, M.M. & Alon, E. Model validation of untethered, ultrasonic neural dust motes for cortical recording. *J Neurosci Methods* **244**, 114-122 (2015).

25. Seo, D. et al. Wireless Recording in the Peripheral Nervous System with Ultrasonic Neural Dust. *Neuron* **91**, 529-539 (2016).

26. Frank, S. & Lauterbur, P.C. Voltage-sensitive magnetic gels as magnetic resonance monitoring agents. *Nature* **363**, 334-336 (1993).

27. Kruttwig, K. et al. Reversible low-light induced photoswitching of crowned spiropyran-DO3A complexed with gadolinium (III) ions. *Molecules* **17**, 6605-6624 (2012).

28. Louie, A. Multimodality imaging probes: design and challenges. *Chem Rev* **110**, 3146-3195 (2010).

29. Weis, R., Müller, B. & Fromherz, P. Neuron adhesion on a silicon chip probed by an array of field-effect transistors. *Phys Rev Lett* **76**, 327-330 (1996).

30. Cohen, A. et al. Depletion type floating gate p-channel MOS transistor for recording action potentials generated by cultured neurons. *Biosensors and Bioelectronics* **19**, 1703-1709 (2004).

31. Lorach, H. et al. Photovoltaic restoration of sight with high visual acuity. *Nat Med* **21**, 476-482 (2015).

32. Palanker, D., Vankov, A., Huie, P. & Baccus, S. Design of a high-resolution optoelectronic retinal prosthesis. *J Neural Eng* **2**, S105-120 (2005).

33. Luo, X.-L., Xu, J.-J., Zhao, W. & Chen, H.-Y. Glucose biosensor based on ENFET doped with SiO2 nanoparticles. *Sens Actuators B Chem* **97**, 249-255 (2004).

34. Miyahara, Y., Moriizumi, T. & Ichimura, K. Integrated enzyme FETs for simultaneous detections of urea and glucose. *Sensors and Actuators* **7**, 1-10 (1985).

35. Hai, A. et al. Acetylcholinesterase-ISFET based system for the detection of acetylcholine and acetylcholinesterase inhibitors. *Biosens Bioelectron* **22**, 605-612 (2006).

36. Lyons, S.K. et al. Noninvasive bioluminescence imaging of normal and spontaneously transformed prostate tissue in mice. *Cancer Res* **66**, 4701-4707 (2006).

37. Evans, M.S. et al. A synthetic luciferin improves bioluminescence imaging in live mice. *Nat Methods* **11**, 393-395 (2014).

38. Juchem, C. & de Graaf, R.A. B0 magnetic field homogeneity and shimming for in vivo magnetic resonance spectroscopy. *Anal Biochem* **529**, 17-29 (2017).

39. U.S. Food and Drug Administration, C.f.D.a.R.H. (U.S. Department of Health and Human Services, 2014).

40. Iwano, S. et al. Single-cell bioluminescence imaging of deep tissue in freely moving animals. *Science* **359**, 935-939 (2018).

41. Ho, J.S. et al. Wireless power transfer to deep-tissue microimplants. *Proc Natl Acad Sci U S A* **111**, 7974-7979 (2014).

42. Lee, H., Sun, E., Ham, D. & Weissleder, R. Chip-NMR biosensor for detection and molecular analysis of cells. *Nat Med* **14**, 869-874 (2008).

43. Haun, J.B. et al. Micro-NMR for rapid molecular analysis of human tumor samples. *Sci Transl Med* **3**, 71ra16 (2011).

44. Kratt, K., Badilita, V., Burger, T., Korvink, J. & Wallrabe, U. A fully MEMS-compatible process for 3D high aspect ratio micro coils obtained with an automatic wire bonder. *J Micromech Microeng* **20**, 015021 (2009).

45. Fischer, A.C. et al. Unconventional applications of wire bonding create opportunities for microsystem integration. *J Micromech Microeng* **23**, 083001 (2013).

46. Feiner, R. & Dvir, T. Tissue–electronics interfaces: from implantable devices to engineered tissues. *Nature Reviews Materials* **3**, 17076 (2017).

47. Eidmann, G., Savelsberg, R., Blümler, P. & Blümich, B. The NMR MOUSE, a mobile universal surface explorer. *Journal of Magnetic Resonance* **122**, 104-109 (1996).

48. Demas, V. et al. Three-dimensional phase-encoded chemical shift MRI in the presence of inhomogeneous fields. *Proc Natl Acad Sci U S A* **101**, 8845-8847 (2004).

49. Cooley, C.Z. et al. Design of sparse Halbach magnet arrays for portable MRI using a genetic algorithm. *IEEE Trans Magn* **54** (2018).

50. Negrin, R.S. & Contag, C.H. In vivo imaging using bioluminescence: a tool for probing graft-versus-host disease. *Nat Rev Immunol* **6**, 484-490 (2006).

51. Naumann, E.A., Kampff, A.R., Prober, D.A., Schier, A.F. & Engert, F. Monitoring neural activity with bioluminescence during natural behavior. *Nat Neurosci* **13**, 513-520 (2010).

52. Hai, A. et al. Changing gears from chemical adhesion of cells to flat substrata toward engulfment of micro-protrusions by active mechanisms. *J Neural Eng* **6**, 066009 (2009).

53. Hai, A. et al. Spine-shaped gold protrusions improve the adherence and electrical coupling of neurons with the surface of micro-electronic devices. *J R Soc Interface* **6**, 1153-1165 (2009).

54. Hai, A., Shappir, J. & Spira, M.E. In-cell recordings by extracellular microelectrodes. *Nat Methods* **7**, 200-202 (2010).

55. Hai, A., Shappir, J. & Spira, M.E. Long-term, multisite, parallel, in-cell recording and stimulation by an array of extracellular microelectrodes. *J Neurophysiol* **104**, 559-568 (2010).

56. Katz, E. & Willner, I. Probing biomolecular interactions at conductive and semiconductive surfaces by impedance spectroscopy: routes to impedimetric immunosensors, DNA-sensors, and enzyme biosensors. *Electroanal* **15**, 913-947 (2003).

57. Hai, A., Cai, L.X., Lee, T., Lelyveld, V.S. & Jasanoff, A. Molecular fMRI of Serotonin Transport. *Neuron* **92**, 754-765 (2016).

FIGURES

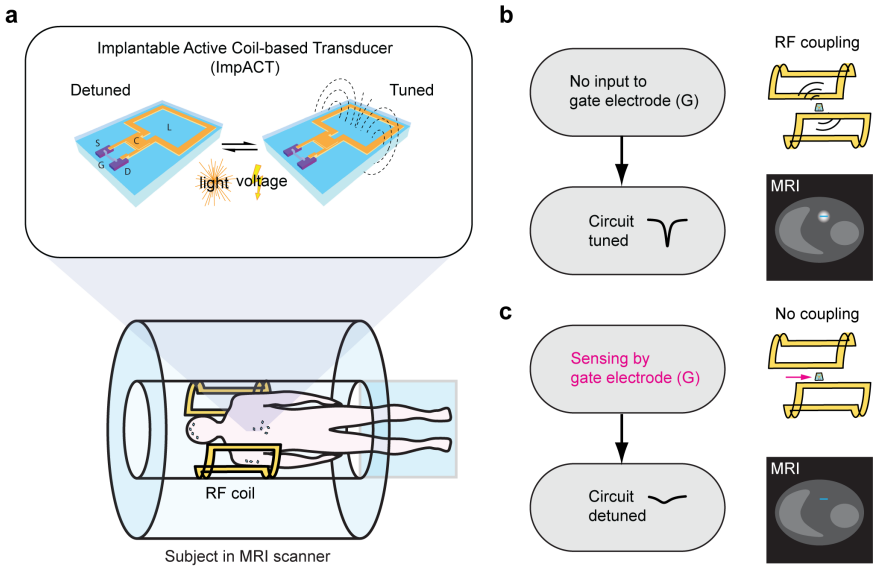

Figure 1. Implantable active coil-based transducers (ImpACTs) as imaging probes for functional MRI. (a) ImpACTs are inductively coupled sensing circuits consisting of a field-effect-transistor (FET, S = source, D = drain, G = gate) in parallel with inductor (L) and capacitor (C); light or voltage input to the gate tunes or detunes the device, altering MRI signal (top). ImpACTs are designed to act as implantable sensors detectable by conventional MRI, potentially in human subjects (bottom). Each ImpACT harvests power from the scanner's RF coil and produces local signal changes modulated by electromagnetic input. **(b)** Operation of an ImpACT tuned to the MRI scanner's resonance frequency, in the absence of input (left). Inductive coupling between the scanner's main RF coil and the ImpACT (top right) allows the device to produce local enhancement in MRI scans (bottom right, blue line denotes ImpACT position). **(c)** Input to the ImpACT gate electrode detunes the device's RF circuit (left), eliminating inductive coupling with the main coil (top right) and causing no MRI signal enhancement near the device (bottom right).

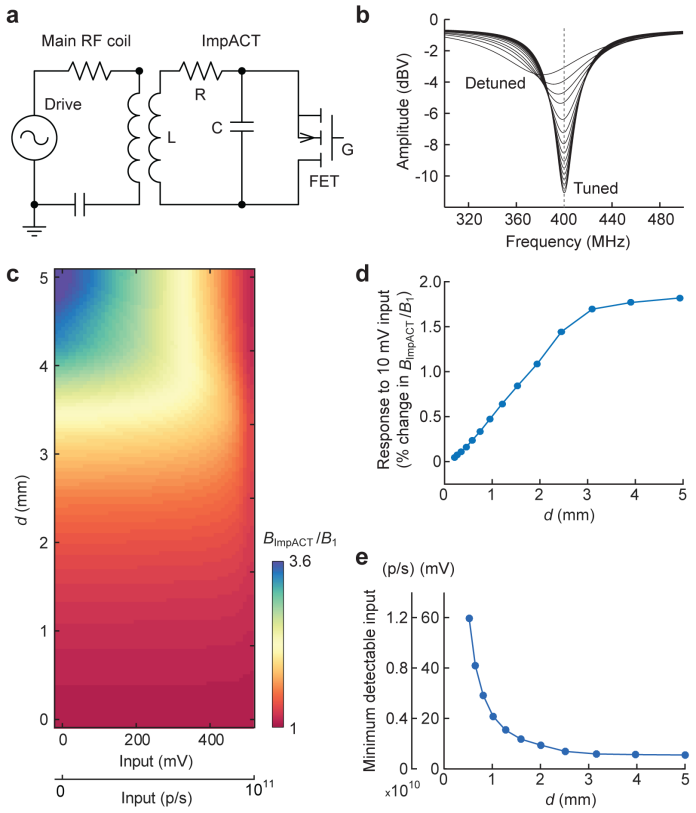

Figure 2. Theoretical performance of ImpACT designs. (a) Equivalent circuit used for simulation of ImpACT devices (right) coupled to an MRI scanner's main RF coil (left). RF pulses generated by the scanner drive the ensemble. Resistor (R), inductor (L), and capacitor (C) of the ImpACT are labeled, as is the device's FET with gate terminal (G). **(b)** ImpACT tuning curve simulations as a function of voltage input that causes the device to vary between fully tuned and fully detuned states (labeled). **(c)** Relative enhancement of local RF amplitude as a function of the ImpACT's inductor diameter (d) and input strength in mV or photons per second (p/s). RF enhancement by the ImpACT is expressed as B_{ImpACT}/B_1, which translates directly into an increase in flip angle during application of an MRI pulse via the scanner's main coil. **(d)** Response to a 10 mV input (also equivalent to 2 x 10^9 p/s), compared with zero input, as a function of the ImpACT inductor diameter. Changes in B_{ImpACT}/B_1 of 1% or greater are likely to be detectable in imaging. **(e)** Minimum photonic and voltaic input signals predicted to produce 1% change or greater in B_{ImpACT}/B_1, compared with zero input, as a function of device diameter.

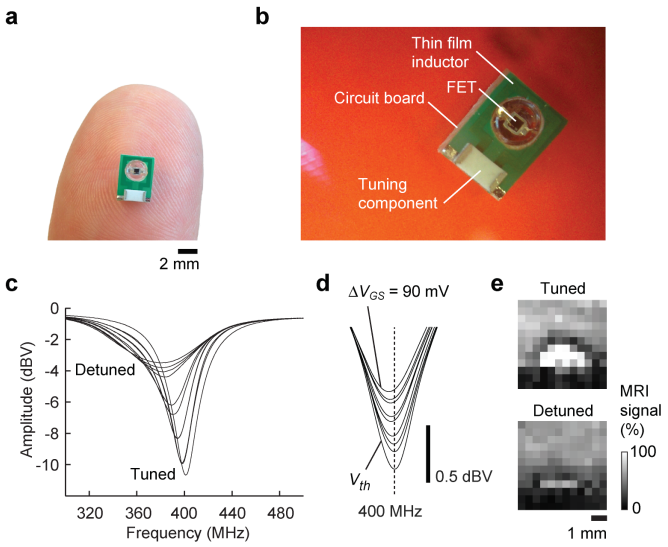

Figure 3. Tuning and imaging performance of an ImpACT prototype. (a) An ImpACT fabricated using standard printed-circuit single turn inductors with 10 µm gold-plated copper as a thin film conductive layer and an inductor of diameter 3 mm, connected in parallel to FET sensor and a tuning component to enable initial resonance frequency at ν = 400 MHz. (**b**) Close-up view of the ImpACT in (a), with components labeled. **(c)** Network analyzer measurements demonstrating ImpACT tuning curves over the full range of FET modulation. FET input was modulated from low ΔV_{GS} ($V_{GS} = V_{th}$) to high ΔV_{GS} (V_{th} + 1 V), resulting in a 3.9-fold decrease of quality factor (Q) from 17.9 to 4.5, comparable to the simulated values in Fig. 2. Inset depicts the actual device. **(d)** Modulation of the ImpACT tuning curve in response to millivolt-scale voltage inputs. The interval between adjacent curves is 10 mV. **(e)** Modulation of MRI signal by light-gated detuning of a photoFET-based ImpACT juxtaposed to a water-based phantom. MRI signal is approximately 30% greater in the absence of input (top) than in the presence (bottom).

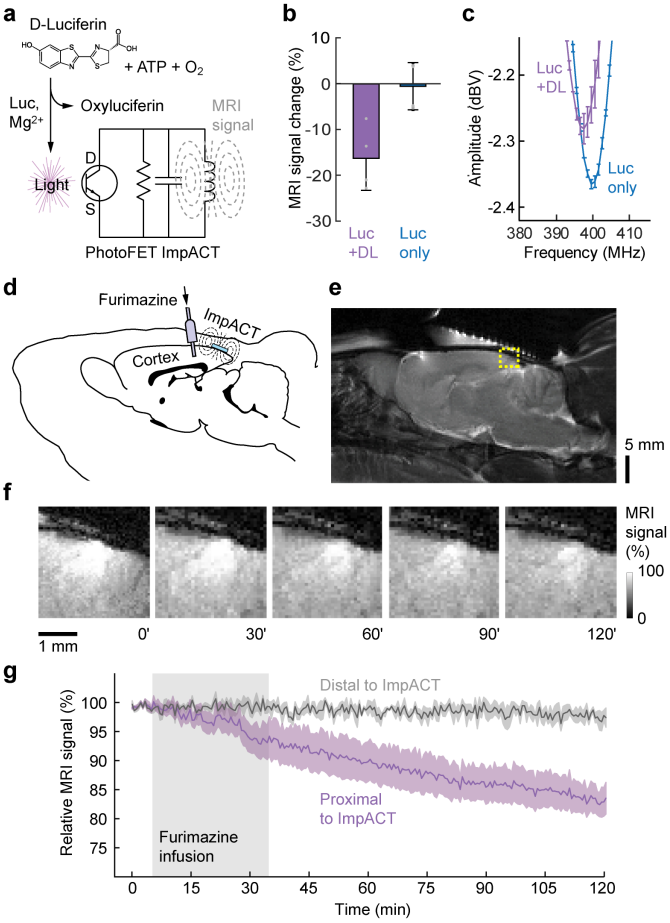

Figure 4. ImpACT-mediated detection of bioluminescence *in vitro* and *in vivo*. (a) Schematic of bioluminescence detection by a photosensitive ImpACT. Luciferase (Luc) in the presence of magnesium ions catalyzes the conversion of D-luciferin, ATP, and O_2 into oxyluciferin and light, which acts on the gate terminal of the ImpACT's photoFET (bottom), altering resonance properties and MRI signal. **(b)** Average MRI signal changes measured using a 3 mm photosensitive ImpACT in the presence of 7.8 μM luciferase with (left) or without (right) addition of D-luciferin (DL). MRI results are reported as percent difference from baseline image intensity distal to the ImpACT. Error bars denote s.e.m. (n = 4); individual measurements indicated by gray dots. **(c)** Measurements of frequency response in the presence and absence of DL, confirming that light production affects MRI signal by detuning the device. Error bars denote s.e.m. (n = 4). **(d)** ImpACT-mediated MRI monitoring of bioluminescent cells in live rat brains. Engineered luciferase (NanoLuc)-expressing HEK-293 cells were grafted into the cerebral cortex. A device was implanted above the cells, and a cannula inserted nearby for infusion of the NanoLuc substrate furimazine. **(e)** Anatomical MRI scan of rat brain showing the region of image signal modulated by the ImpACT (dashed yellow box). **(f)** Close-up images obtained at t = 0, 30, 60, 90 and 120 minutes before, during, and after furimazine infusion (t = 5-35 mins). Signal enhancement in the center of this region reflects the presence of the tuned ImpACT device; the enhancement dims over time as the ImpACT is progressively detuned by luminescence from the implanted cells. **(g)** Mean time courses of relative MRI signal proximal (purple) and distal (gray) to the ImpACT (shaded intervals denote s.e.m. over four animals). Furimazine infusion period indicated by gray box. Control experiments with injections lacking furimazine showed no discernable signal changes (**Supplementary Fig. 10**).

SUPPLEMENTARY INFORMATION

Table of Contents **page**

SUPPLEMENTARY TEXT

Additional ImpACT design considerations

To evaluate the ImpACT circuit metal layer thickness (t_m) required for sensing electrical or photonic input, we simulated the response of devices with feasible t_m values ranging between 500 nm and 10 μm. Throughout most of this range, reducing t_m increases the impedance of its inductor component, lowering the device's Q and reducing the coupling efficiency between the ImpACT and the MRI coil. **Supplementary Fig. 2** shows that this has the effect of reducing the change in B_{ImpACT}/B_1 that can be achieved by modulating inputs to the device, lowering its sensitivity. For devices with t_m greater than 8 μm (thicker than twice the skin depth at 400 MHz), performance is approximately constant, with inputs producing up to 63% changes in B_{ImpACT}/B_1. For $t_m < 1$ μm, no discernable change in B_{ImpACT}/B_1 can be produced however.

Although the simulated data of **Fig. 2** and **Supplementary Fig. 2** establish lower bounds of $d = 1$ mm and $t_m = 1$ μm on the fabrication of sensitive ImpACT devices produced with single turn inductors and commercially available compact FETs, we examined additional design factors that could permit improved sensitivity or further miniaturization of the devices in future work. **Supplementary Fig. 3** shows that one route to achieving improved sensitivity is to increase the FET or photoFET's transconductance (g_m), defined as the reciprocal of its drain-source resistance in the fully open state. By increasing g_m fourfold from the value of 5×10^{-3} used in the simulations of **Fig. 2**, the predicted response of a 1 mm ImpACT to a 10 mV input increases by 79%, and the minimum detectable input reaches 11.3 mV or 2.3×10^9 p/s.

A second strategy for improving sensitivity involves increasing the number of turns of the ImpACT inductor coil. **Supplementary Fig. 4** shows that devices with diameters 1 mm, 500 μm, 250 μm, and 100 μm, can achieve 1% changes in B_{ImpACT}/B_1 in response to inputs of 5.6 mV, 5.8 mV, 9.9 mV, and 33 mV respectively.

SUPPLEMENTARY FIGURES

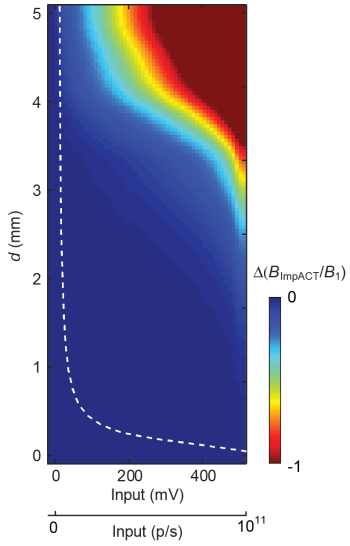

Supplementary Figure 1. Change in enhancement of local RF field intensity as a function of ImpACT dimensions and input strength. MRI effects are modeled as enhancements to the local RF field in the neighborhood of the ImpACT device (B_{ImpACT}/B_1). This graph shows the change in B_{ImpACT}/B_1 at each input amplitude (mV or p/s), with respect to zero input, for each value of the device diameter (d). The white dashed line denotes minimum inputs required to produce 1% change in B_{ImpACT}/B_1, with respect to zero input, for each value of d.

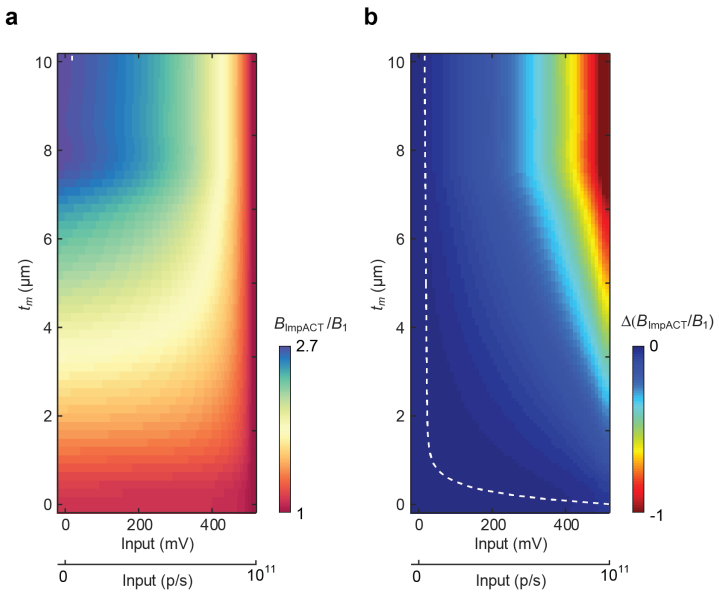

Supplementary Figure 2. Enhancement of local RF intensity as a function of film thickness and input strength. (a) MRI effects are modeled as enhancements to the local RF field in the neighborhood of the device (B_{ImpACT}/B_1), as a function of the ImpACT film thickness (t_m) and the gate input strength in mV or p/s, assuming a device diameter of d = 3 mm. For t_m < 8 μm, the difference between MRI signal in the low *vs.* high input states decreases rapidly, and for t_m < 1 μm falls below the estimated detection limit of 1% change in B_{ImpACT}/B_1 for the entire input range. This sets a lower bound on t_m necessary for constructing effective ImpACT sensors. **(b)** The same results shown as the change in B_{ImpACT}/B_1 at each input amplitude, with respect to zero input, for each value of t_m. The white dashed line denotes minimum inputs required to produce 1% change in B_{ImpACT}/B_1, with respect to zero input, for each value of t_m.

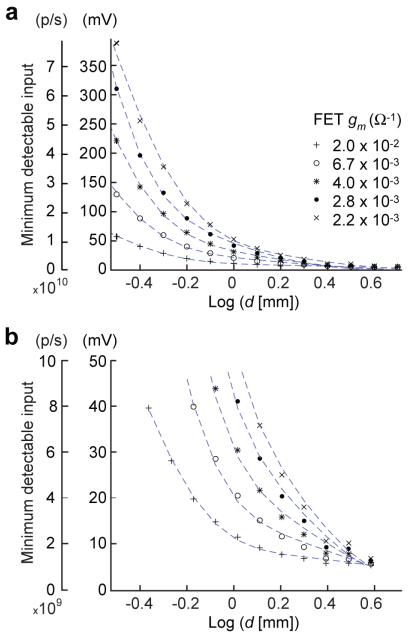

Supplementary Figure 3. ImpACT sensitivity as a function of FET transconductance. Minimum photonic and voltaic input signals predicted to produce 1% change or greater in B_{ImpACT}/B_1 were computed as a function of device diameter (d) for various transconductance (g_m) values shown. Panel **(a)** shows the full range of sensitivities for devices of d = 0.3 to 4 mm; **(b)** depicts the same data, zoomed in to emphasize sensitivities in the 0–50 mV (0–10^{10} p/s) range.

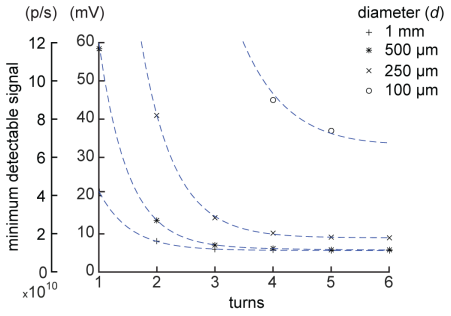

Supplementary Figure 4. Sensitivity of submillimeter multiturn ImpACT devices to voltaic and photonic inputs. Multiturn ImpACTs with diameters 1 mm, 500 µm, 250 µm, and 100 µm, can achieve 1% changes in B_{ImpACT}/B_1 in response to inputs of -5.6 mV, -5.8 mV, -9.9 mV, and -33 mV, respectively.

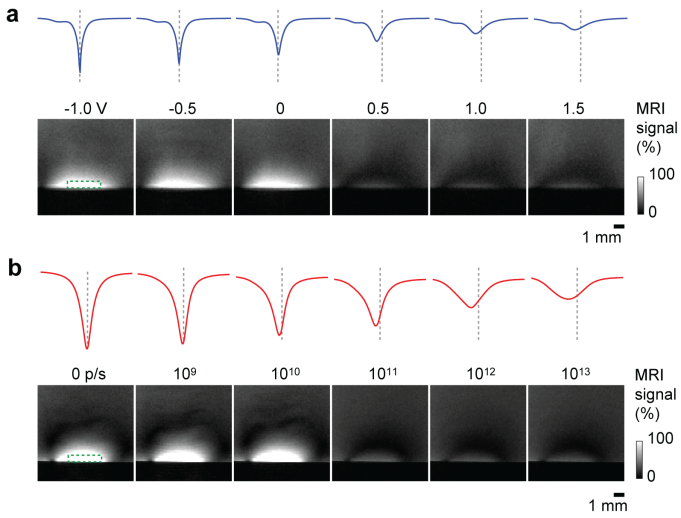

Supplementary Figure 5. Sensitivity of ImpACTs to biologically relevant fields. ImpACTs are initially tuned to resonance frequency of v = 400 MHz, in the absence of input at the FET closed state, and are detuned by input to gate electrode. **(a)** Application of voltage above V_{th} detunes the device and decreases Q (tuning curves at top), causing a reduction of MRI signal (images at bottom). ΔV_{GS} values shown for each condition, and 400 MHz frequency denoted vertical dotted lines with each tuning curve. **(b)** Photonic input from 0–10^{13} p/s into a photoFET-based ImpACT device produces similar responses as the voltage input in panel (a).

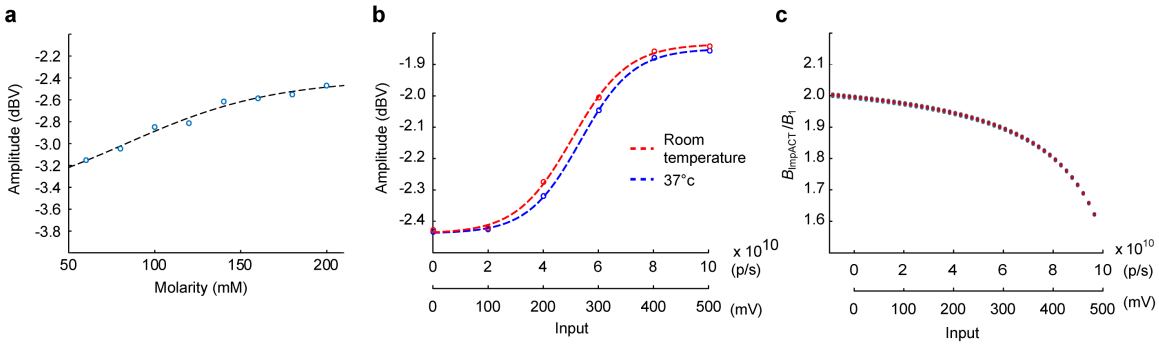

Supplementary Figure 6. ImpACT sensitivity to environmental changes. (a) Experimentally-determined dependence on ionic strength. A 3 mm ImpACT was initially tuned to resonance frequency ν = 400 MHz and juxtaposed to saline solutions of 60-200 mM. Graph shows tuning depth (dBV) at the resonance frequency for different molarity values. **(b)** Temperature-dependence of ImpACT responses to stimulation. Tuning behavior against a 150 mM saline sample was measured across the entire dynamic range of inputs at room temperature (22 °C, red) or 37 °C (blue). **(c)** Simulated ImpACT response profiles predicted for operation at small frequency offsets from the main field resonance frequency (400 MHz). Curves determined over a range of offsets from 399 to 401 MHz are superimposable, showing negligible effect of realistic field distortions of up to 2,500 parts per million.

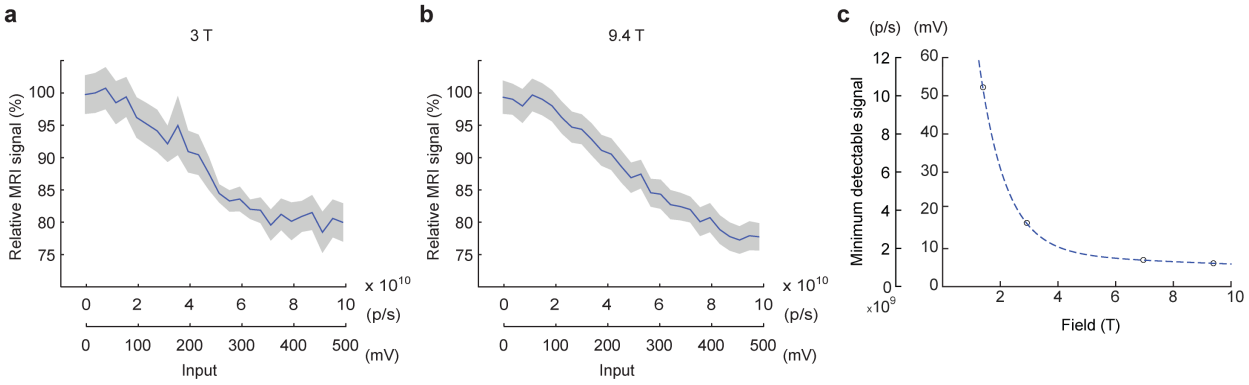

Supplementary Figure 7. ImpACT sensitivity at different MRI field strengths. (a) A 3 mm ImpACT tuned to v = 123.2 MHz was operated in a 3T clinical scanner over the full range of input amplitudes. **(b)** An ImpACT tuned to 400 MHz was similarly operated on a 9.4 T scanner. Shading denotes s.e.m. over 8 voxels in proximity to the ImpACT. **(c)** Simulated sensitivity of ImpACT devices, defined as the input amplitude predicted to produce a 1% change in B_{ImpACT}/B_1, as a function of magnetic field strength.

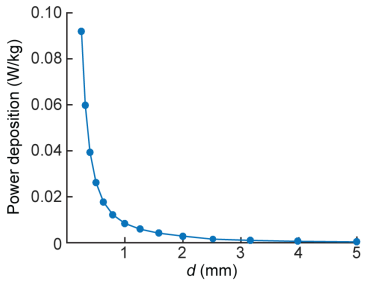

Supplementary Figure 8. Maximum local specific power dissipation by ImpACT devices. For ImpACT devices of different diameters (*d*), we calculated an upper bound on the local specific absorbance rate by computing the maximum specific power deposited in the ImpACT and then assuming that this power is transferred to a spherical volume of tissue of twice the diameter of the device (see Methods for details).

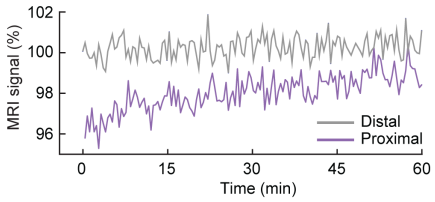

Supplementary Figure 9. Time course of relative MRI signal produced by NanoLuc-expressing cells. The graph shows time courses of NanoLuc-expressing HEK293 cells placed in close juxtaposition to an ImpACT device, following addition of 5 μM furimazine. Signal close to the device (purple) shows relative suppression due to detuning of the device, compared with distal MRI signal (gray), which is not affected by the ImpACT or its tuning status.

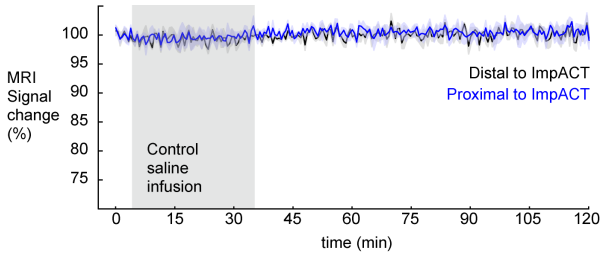

Supplementary Figure 10. MRI monitoring of ImpACT response to sham injections of saline in live rat brains. Control experiments were performed as in Fig. 4g, but with injection of saline solution instead of furimazine. Engineered luciferase (NanoLuc)-expressing HEK-293 cells were grafted into the cerebral cortex and ImpACT device was implanted above the cells. An infusion cannula was inserted nearby for infusion of saline. Saline infusion (t = 5-35 mins) resulted in no significant signal enhancement in the center of the ImpACT device (paired t-test p = 0.9309) which remained tuned throughout the experiments. Mean time course depicts relative MRI signal proximal (blue) and distal (black) to the ImpACT (shaded margins denote s.e.m. over three animals). Saline infusion period indicated by gray box. Signal change axis spans 70-100 % as in Fig. 4g.

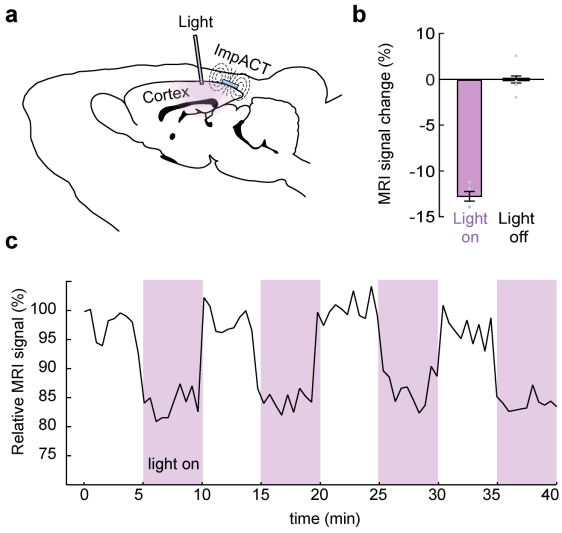

Supplementary Figure 11. Reversible detuning of an ImpACT device in live rat brain. **(a)** A 3 mm photosensitive ImpACT device was implanted above the cortical surface of an anesthetized rat and an optical fiber was inserted 1 mm anterior to implantation site for light-dependent modulation. **(b)** Application of 5 x 10^{10} p/s generated MRI signal decrease of 12.7 ± 0.7 % in cortical region proximal to the device. Bars denote mean values, error bars denote s.e.m. (n = 4); individual data measurements indicated by gray dots. **(c)** Relative MRI signal proximal to ImpACT device in response to intermittent application of 5 x 10^{10} p/s through the optical fiber. Purple shaded areas denote 5 min epochs of light application.